Acta Astronautica 241 (2026) 608–619

Contents lists available at ScienceDirect

Acta Astronautica

journal homepage: www.elsevier.com/locate/actaastro

Kinematic orbit determination for BDS-3 satellites with inter-satellite link data

Chao Yang [a], Jing Guo [b,*], Xiaolong Mi [a], Yuanfan Deng [a], Xuexi Liu [c], Qile Zhao [b], Wu Chen [a]

[a] Department of Land Surveying and Geo-Informatics, The Hong Kong Polytechnic University, 999077, Hong Kong, China
[b] GNSS Research Center, Wuhan University, No. 129 Luoyu Road, Wuhan, 430079, China
[c] School of Environment Science and Spatial Informatics, China University of Mining and Technology, Xuzhou, 221116, China

ARTICLE INFO

Keywords:
BDS-3
Kinematic orbits
Inter-satellite link
Precise orbit determination

ABSTRACT

Kinematic orbit determination offers an efficient and highly accurate alternative to traditional methods by eliminating the need for time-consuming orbit integration and complex satellite dynamics modeling (e.g., solar radiation pressure, earth radiation pressure, etc.). Leveraging the Ka-band inter-satellite link (ISL) payloads deployed on the BeiDou global navigation satellite system (BDS-3), this study presents, for the first time, kinematic orbit determination results for BDS-3 satellites using real ISL measurements. The analysis reveals that the position dilution of precision (PDOP) for Medium Earth Orbit (MEO) satellites ranges from 0.8 to 2.0, while for Inclined Geosynchronous Orbit (IGSO) and Geostationary (GEO) satellites, PDOP values remain within 1.2–2.5 and 1.2–2.0, respectively. The mean 3D RMS values of kinematic orbits are approximately 13.6 cm, 23.5 cm, and 33.7 cm for MEO, IGSO and GEO satellites, respectively, when the orbits of all satellites except one are constrained to the precise dynamic solutions. The mean cross-track accuracy of BDS-3 satellites is 7.3 cm, which is more than 1.5 cm larger than that of the along-track and radial directions. Furthermore, this work systematically investigates the impact of the number of fixed satellites on kinematic solutions, demonstrating that fixing two satellites improves orbit accuracy by 29 % over fixing just one, and that constraining all IGSO and GEO satellites yields optimal results for MEO satellites, with mean 3D RMS values of 15.8 cm (along-track), 14.5 cm (cross-track), and 14.0 cm (radial). Notably, the kinematic orbit accuracy remains robust, as no significant decrease is detected during eclipse seasons.

1. Introduction

In the 1980s, the concept of utilizing inter-satellite links (ISL) for autonomous navigation was first proposed [1]. Subsequently, the United States launched the GPS Block IIR spacecraft with Ultra-High Frequency (UHF) wide-beam antennas in 1997 [2]. The experiments revealed that, with 75 days of independent orbit determination using ISL data, the satellites maintained a user range error (URE) under 3 m [3]. Due to the Ka-band's higher ranging accuracy and stronger anti-jamming capability, it replaces the UHF-band for GPS Block III satellites to build ISL [4]. Although the ISL of the Galileo system has not yet been implemented, ISL-related evaluations and technical demonstrations were also carried out. The European Space Agency (ESA) conducts two projects (ADVISE and GNSS+) to evaluate ISL, inter-satellite communications, and onboard orbital clock offset determination capabilities [5]. In addition, based on the Galileo system, the German Aerospace Center (DLR) introduced the concept of a next-generation GNSS constellation, i.e., "Kepler", which plans to exploit optical ISL instead of microwave ISL and adds Low Earth Orbit (LEO) links to enable a perfect time synchronization [6,7]. Michalak et al. [8] conducted comprehensive simulations, demonstrating a significant enhancement in orbit accuracy.

Compared with the other systems, the ISL is much more essential for the BeiDou satellite navigation system (BDS). Research efforts focused on ISL routing, networking technologies, and autonomous orbit determination for navigation satellites were initiated around ten years ago [9–11]. Since 2015, five BDS experimental satellites carrying Ka-band array antennas have been launched to verify ISL technology. Zhou et al. [12] have shown that ISL accuracy can reach 10 cm. Ren et al. [13] demonstrated that orbits with meter-level accuracy can be obtained by using solely ISL observations and imposing precise a priori orbit constraints. The integration of Ka-band and ground L-band data can further enhance BDS satellite orbits quality, particularly when only a few

* Corresponding author.
E-mail address: jingguo@whu.edu.cn (J. Guo).

https://doi.org/10.1016/j.actaastro.2026.01.015
Received 26 September 2025; Received in revised form 24 November 2025; Accepted 5 January 2026
Available online 6 January 2026

regional stations are available [14,15].

Afterward, ISL technology was fully applied to BDS-3, including Medium Earth Orbit (MEO), Inclined Geosynchronous Orbit (IGSO) and Geostationary (GEO) satellites, which officially provided global services on July 31, 2020. The regional monitoring stations cannot fully track BDS-3 MEO and IGSO satellites, and the observation geometry for GEO is almost static, making the orbit quality low. The ISL can overcome these shortcomings and improve the orbit accuracy, particularly broadcast ephemeris. Lv et al. [16] assessed the orbit errors of BDS-3 satellites and found them to be at the 0.1 m level. With ISL observations from eight satellites, the 3D overlapping errors of orbits were reduced to 0.5 m, using ten regional stations [17]. When additional links and stations are incorporated, Satellite Laser Ranging (SLR) residuals show that the orbit accuracy of BDS-3 MEO satellites can reach 2–5 cm [18–21]. Meanwhile, the overlapping errors for IGSO and GEO satellites are about 12 cm and 18 cm, respectively [22,23]. Furthermore, the ISL-based autonomous orbit determination method for GEO satellites proposed by Jiao et al. [24] can achieve sub-meter level accuracy.

All the above-listed studies on precise orbit determination (POD) for BDS-3 are based on the dynamic approach. The dynamic solutions are vulnerable to the effect of orbit perturbations. In particular, the performance of the non-gravitational forces modelling (solar radiation, earth radiation, etc.) is crucial for the dynamic orbit [25]. Kinematic orbit determination for LEO satellites is predominantly achieved through satellite-to-satellite tracking utilizing onboard GNSS receivers. Since these orbits are computed directly from GNSS measurements, no dynamic force models are employed in the determination process [26]. Usually, this approach is not used for GNSS satellites, as the geometry condition is worse, making the dilution of precision (DOP) up to several times higher. However, in contrast from the ground or LEO onboard L-band data, the ISL measures the range with a few centimeters accuracy between MEO, IGSO, and GEO satellites, and provides better observation conditions. Hence, it has the potential to determine kinematic orbit solutions with high accuracy and more efficiency, as the time-consuming numerical orbit integration can be omitted.

In this research, the possibility of kinematic orbit determination based on ISL data for BDS-3 is explored. First, the description of BDS-3 satellites, as well as the ISL measurement and its connectivity scheme are presented, following the POD strategy used, as well as the DOP analysis. Subsequently, the kinematic orbits are determined and analyzed by investigating on the impacts of fixed orbits and the performance in the eclipse seasons. Finally, the conclusion and discussion are presented.

2. Characteristics of ISL

The BDS-3 constellation comprises 30 satellites developed by the China Academy of Space Technology (CAST) and the Shanghai Engineering Center for Microsatellites (SECM) under the Chinese Academy of Sciences. Table 1 shows that the 24 MEOs are positioned on three distinct planes—Plane-A, Plane-B, and Plane-C. The 3 IGSOs and 3 GEOs are distributed on their respective orbital planes. Fig. 1 shows the trajectory of the subsatellite point for the selected satellites on each orbital plane, i.e., C27, C19, C23, C38, C39, C40 and C59. All BDS-3 spacecraft have inter-satellite ranging capabilities with Ka-band antennas. ISLs are established using Concurrent Spatial Time Division (CSTD) technology [15]. The entire constellation can establish many links at the same time, but there is only one for each satellite in one timeslot, i.e., 3 s. This is the concurrency mechanism. Through the time division mechanism, each satellite connects with other satellites at separate timeslots. The satellites track each other in the range of limited nadir angles (−60°, 60°) by varying the beam direction, which realizes spatial division. The rapid tracking capability of the phased array antenna enables it to perform dual one-way ranging efficiently within a short period, following the preassigned timeslot schedule. That is, the forward and backward links are finished in the first and second 1.5 s, respectively. Theoretically, 20 links are formed across the whole constellation. Thus, there are adequate links within the whole constellation for orbit determination.

Table 1
Overview of BDS-3 satellites.

Manufacturer	Orbit	Satellite
CAST	Plane-B	C19, C20, C21, C22, C32, C33, C41, C42
SECM	Plane-A	C27, C28, C29, C30, C34, C35, C43, C44
CAST	Plane-C	C23, C24, C36, C37, C45, C46
SECM	Plane-C	C25, C26
CAST	IGSO	C38, C39, C40
	GEO	C59, C60, C61

To show the connection scheme of BDS ISL, Fig. 2 depicts the status of ISL connections for C20, a MEO in the B-plane. It connects continuously with C21, C22, C25, C28, C33, C41, C44, and C45, but other satellites are intermittently visible with C20. Given the limitations of the nadir angle and the obstruction caused by the Earth, in-plane links cannot be formed between adjacent satellites as well as the satellites with the farthest distance. Hence, one satellite can be continuously linked with four satellites in its own orbital plane. Additionally, four continuously visible out-of-plane links can also be formed, and the remaining links are intermittently visible.

3. Methodology

3.1. ISL mathematical model

Suppose that satellite A and satellite B complete the dual one-way observation in one timeslot, i.e., 3 s. Satellite A and satellite B receive signals at t_1 and t_2, respectively, and the raw observation equations for the dual one-way ISL are given by:

$$P_{BA}(t_1) = \left|\overrightarrow{R}_A(t_1) - \overrightarrow{R}_B(t_1 - \Delta t_1)\right| + c\cdot(\delta t_A(t_1) - \delta t_B(t_1 - \Delta t_1)) + c\cdot\left(\tau_A^R + \tau_B^S\right) + \Delta\delta_{BA} + \varepsilon_{BA} \tag{1}$$

$$P_{AB}(t_2) = \left|\overrightarrow{R}_B(t_2) - \overrightarrow{R}_A(t_2 - \Delta t_2)\right| + c\cdot(\delta t_B(t_2) - \delta t_A(t_2 - \Delta t_2)) + c\cdot\left(\tau_B^R + \tau_A^S\right) + \Delta\delta_{AB} + \varepsilon_{AB} \tag{2}$$

Where $P_{BA}(t_1)$ is the ISL measurement from satellite B to satellite A at epoch t_1. $P_{AB}(t_2)$ is the ISL measurement from satellite A to satellite B at t_2. c denotes the speed of light in a vacuum. Δt_1 and Δt_2 refer to the propagation time. $\overrightarrow{R}_A(t_1)$ and $\overrightarrow{R}_A(t_2 - \Delta t_2)$ are the position vectors of satellite A at epochs t_1 and $t_2 - \Delta t_2$; similarly, $\overrightarrow{R}_B(t_2)$ and $\overrightarrow{R}_B(t_1 - \Delta t_1)$ are the position vectors of satellite B at epochs t_2 and $t_1 - \Delta t_1$. $\delta t_A(t_1)$ and $\delta t_A(t_2 - \Delta t_2)$ are the clock offsets of satellite A at the epochs t_1 and $t_2 - \Delta t_2$, while $\delta t_B(t_2)$ and $\delta t_B(t_1 - \Delta t_1)$ represent the clock offsets of satellite B at the epoch t_2 and $t_1 - \Delta t_1$. τ_A^R and τ_A^S denote the receiving and transmitting hardware delays for satellite A, while τ_B^R and τ_B^S denote the receiving and transmitting hardware delays for satellite B. These delay parameters are assumed to be constant. $\Delta\delta_{BA}$ and $\Delta\delta_{AB}$ are the corrections, including Ka-band antenna phase offsets, gravitational time delay and relativistic effect caused by orbital eccentricity. ε_{BA} and ε_{AB} represent the noise in the one-way ISL measurement, which is on the order of 1∼3 cm [17].

Usually, the dual nonsynchronous one-way observations, $P_{BA}(t_1)$ and $P_{AB}(t_2)$, are converted to the observables $P_{BA}(t_0)$ and $P_{AB}(t_0)$ at the same epoch t_0 with corrections ΔP_{BA} and ΔP_{AB} as follows:

$$P_{BA}(t_0) = P_{BA}(t_1) + \Delta P_{BA} \tag{3}$$

$$P_{AB}(t_0) = P_{AB}(t_2) + \Delta P_{AB} \tag{4}$$

where ΔP_{BA} and ΔP_{AB} can be obtained as follows:

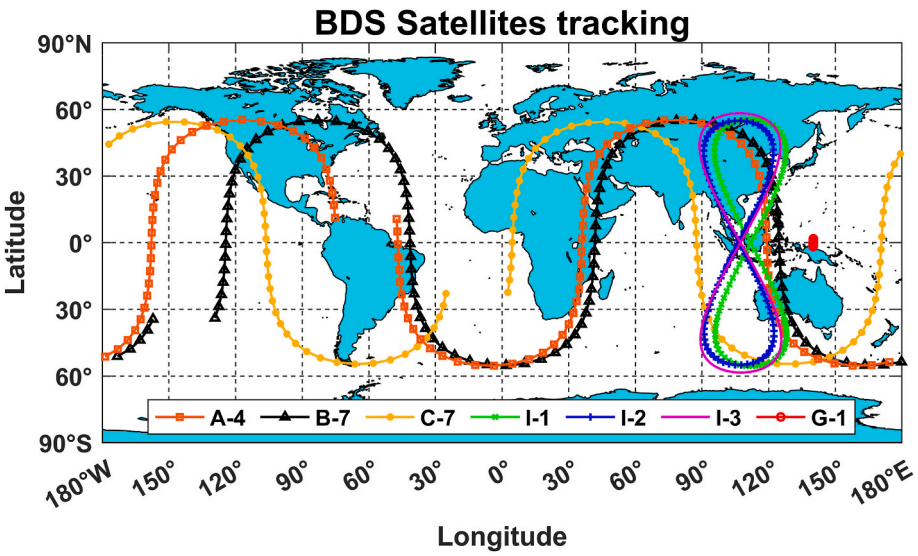

Fig. 1. Trajectories of sub-satellite points for the selected MEO, IGSO, and GEO satellites on each orbital plane. C27 (A-4), C19 (B-7) and C23 (C-7) are located on the plane A, B, and C of the MEO, respectively. The green, blue, manganese purple and red represent C38, C39, C40 and C59, respectively. (For interpretation of the references to color in this figure legend, the reader is referred to the Web version of this article.)

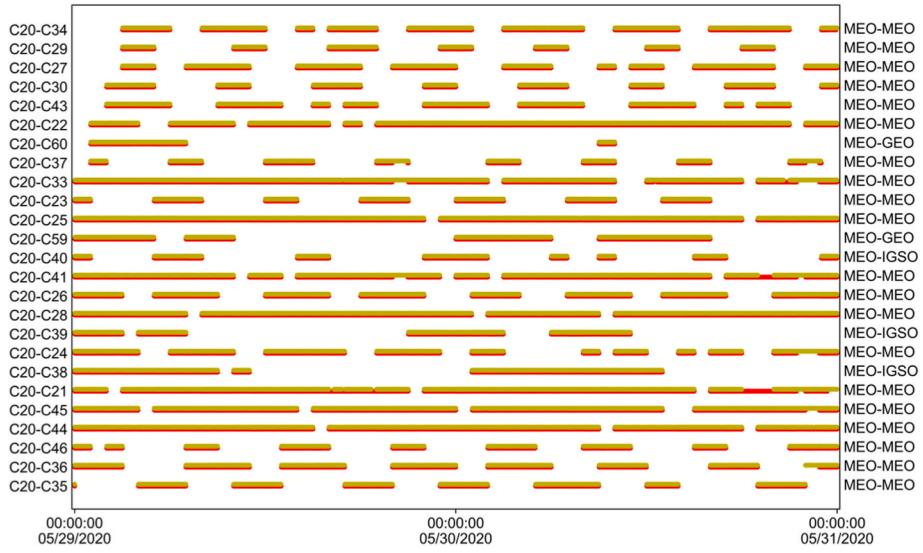

Fig. 2. ISL connections for C20 during DOY 150–151, 2020. The red and yellow represent the forward and backward observations, respectively. (For interpretation of the references to color in this figure legend, the reader is referred to the Web version of this article.)

$$\Delta P_{BA} = P_{BA}(t_0) - P_{BA}(t_1) = \left|\vec{R}_A(t_0) - \vec{R}_B(t_0)\right| - \left|\vec{R}_A(t_1) - \vec{R}_B(t_1 - \Delta t_1)\right| + c \cdot (\delta t_A(t_0) - \delta t_B(t_0)) - c \cdot (\delta t_A(t_1) - \delta t_B(t_1 - \Delta t_1)) \tag{5}$$

$$\Delta P_{AB} = P_{AB}(t_0) - P_{AB}(t_2) = \left|\vec{R}_B(t_0) - \vec{R}_A(t_0)\right| - \left|\vec{R}_B(t_2) - \vec{R}_A(t_2 - \Delta t_2)\right| + c \cdot (\delta t_B(t_0) - \delta t_A(t_0)) - c \cdot (\delta t_B(t_2) - \delta t_A(t_2 - \Delta t_2)) \tag{6}$$

where $\vec{R}_A(t_0)$ and $\vec{R}_B(t_0)$ are the position vectors of satellites A and B at epoch t_0, and $\delta t_A(t_0)$ and $\delta t_B(t_0)$ are the clock offsets of satellites A and B at epoch t_0. These can be calculated from the broadcast ephemeris and the clock. The error induced by the reduction does not exceed 1 cm, as the accuracy of the satellite velocity is at the level of 0.1 mm/s and the accuracy of the satellite clock drift is better than 1×10^{-13} s/s [27]. Hence, the error introduced by the above transformation can be ignored [15]. When taking (5) and (6) into (1) and (2), the observation equation for $P_{BA}(t_0)$ and $P_{AB}(t_0)$ can be derived as follows:

$$P_{BA}(t_0) = \left|\vec{R}_A(t_0) - \vec{R}_B(t_0)\right| + c \cdot (\delta t_A(t_0) - \delta t_B(t_0)) + c \cdot \left(\tau_A^R + \tau_B^S\right) + \Delta\delta_{BA} + \varepsilon_{BA} \tag{7}$$

$$P_{AB}(t_0) = \left|\vec{R}_B(t_0) - \vec{R}_A(t_0)\right| + c \cdot (\delta t_B(t_0) - \delta t_A(t_0)) + c \cdot \left(\tau_B^R + \tau_A^S\right) + \Delta\delta_{AB} + \varepsilon_{AB} \tag{8}$$

By adding (7) and (8), the clock-free observation $P(t_0)$ can be obtained and used for kinematic orbit determination as follows:

$$P(t_0)=\frac{P_{BA}(t_0)+P_{AB}(t_0)}{2}=\left|\vec{R}_A(t_0)-\vec{R}_B(t_0)\right|+c\cdot(\delta_A+\delta_B)+\varepsilon \tag{9}$$

where $\delta_A=\left(\frac{\tau_A^R+\tau_A^S}{2}\right)$, $\delta_B=\left(\frac{\tau_B^R+\tau_B^S}{2}\right)$ and $\varepsilon=\frac{\varepsilon_{BA}+\varepsilon_{AB}}{2}$. This means that the receiving and transmitting hardware delays of each satellite are combined into one satellite-specific constant parameter for estimation. For simplicity, the systematic error terms have been omitted in the above equation.

3.2. Dilution of precision

Dilution of Precision (DOP) factors are commonly used to characterize how receiver-transmitter geometry influences the accuracy of kinematic orbit determination. DOP factors are straightforward functions of the diagonal elements of the covariance matrix for the adjusted parameters, which are obtained from the linearized model. Generally,

$$\sigma=\sigma_0 DOP \tag{10}$$

where σ_0 denotes the standard derivation (STD) of the observed ISL measurements, and σ is a scalar indicator of the positioning STD. When the DOP is computed, the ISL measurements are assumed to be uncorrelated and have identical accuracy. The cofactor matrix of the adjusted position Q_x can be written as:

$$Q_x=\left(A^TA\right)^{-1}=\begin{bmatrix} q_x & q_{xy} & q_{xz} \\ q_{yx} & q_y & q_{yz} \\ q_{zx} & q_{zy} & q_z \end{bmatrix} \tag{11}$$

where A is the design matrix obtained by linearizing the (9). The DOP factors depend on the diagonal elements of (11). Hence, the position dilution of precision (PDOP) can be obtained as follows:

$$PDOP=\sqrt{q_x+q_y+q_z} \tag{12}$$

For satellites, results are frequently interpreted in the local orbital coordinate system, comprising the along-track, cross-track, and radial axes. As PDOP serves only as a measure of positioning accuracy, the cofactor matrix is therefore not transformed to the orbital reference frame.

3.3. Strategy

First, the L-band data collected from 100 stations from the International GNSS Service (IGS) and the International GNSS Monitoring And Assessment System (iGMAS) are combined with the ISL data to determine the orbits for BDS-3 MEO, IGSO, and GEO satellites based on the dynamic approach with a similar strategy as that of WUM products [28, 29]. The determined dynamic orbits are used as the reference for performance validation of kinematic orbit solutions. The SLR residuals of MEO satellites are approximately 2-4 cm [20], and the 48-h overlapping errors of IGSO satellites are around 10 cm [23].

For kinematic orbit determination, the ISL-only data from day of year (DOY) 125–177, 2020, with 60 s intervals are processed based on the modified Position and Navigation Data Analyst (PANDA) software [30]. Sufficient measurement data is necessary for successful kinematic orbit determination. To meet the requirement, the dual one-way ISL observations are processed into the inter-satellite ranges at the epoch of the integer minute. As the timeslot is 3 s, there are 20 observables available within a 60 s interval for orbit determination, in theory. Nevertheless, because of discontinuous connections and data gaps, the actual number falls below 20. Fig. 3 illustrates the variation of ISL observations for C24 on DOY 165, 2020. In most cases, more than 12 observations are present at each epoch. Other satellites show similar patterns.

As only the ISL data between satellites are used, the atmospheric delay is completely omitted. Regarding the phase center offsets (PCO) of Ka-band antennas, the manufacture values are employed. The attitude models developed by Wang et al. [31] and Yang et al. [32] are utilized to CAST IGSO and MEO satellites, and SECM MEO satellites, respectively, whereas the orbit-normal mode is assumed for GEO satellites. The relativistic effects and gravitational corrections follow the IERS Conventions 2010. The 24-h data are used to estimate the epoch-wise orbits without constrains between epochs, while the satellite-specific

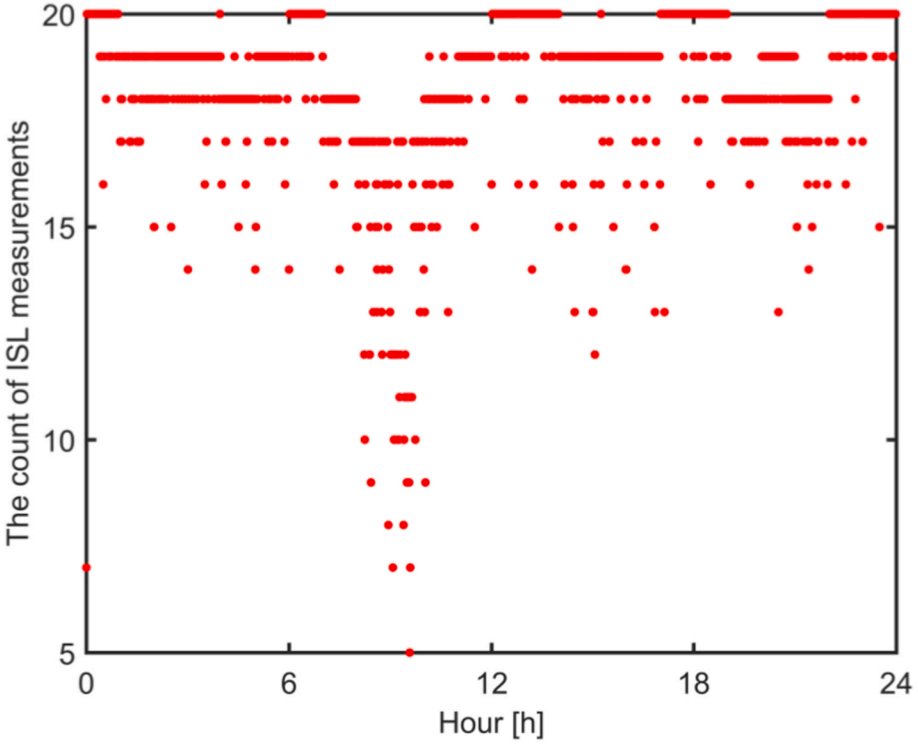

Fig. 3. The variation in the ISL observation count on DOY 165, 2020, for C24.

hardware delays are estimated as arc-dependent constants. The least square algorithm is used in post-processing. Table 2 presents the characteristics of the kinematic method.

4. Results

4.1. PDOP analysis

To predict the kinematic orbit accuracy, the PDOP is calculated for one selected day, i.e., DOY 171, 2020, based on (12). Fig. 4 presents the PDOP timeseries of BDS-3 satellites in each orbital plane. It is clearly observed that the superior observation geometry of the MEO satellites, relative to the IGSO and GEO satellites, as the PDOP varies mainly in the range of 0.8–2.0. The satellites on the Plane A, B and C have almost the same observation geometry. For IGSO satellites, the PDOP varies between 1.2 and 2.5. The PDOP of C59 shows relatively stable variations within the range of 1.2–2.0. The jumps of the PDOP are caused by the sudden reduction of the count of observations, possibly due to the interruption in the downward transmission of the ISL data.

The ISL measurement noise, as shown in Fig. 5, is obtained by linearly fitting the 1-h orbit-free ISL observables. It is evident that satellites in Plane-A have greater measurement noise than those in Plane-B. In the Plane-C, except for satellites C23, C25, and C26, the noise of other satellites is comparable to that of satellites in the Plane-B. IGSO and GEO satellites exhibit a measurement noise of roughly 2 cm. The noise level of CAST satellites, at 3 cm, is higher than that of SECM satellites, which is at 2 cm. According to equation (10), taking 3 cm as the STD of the observed ISLs and a PDOP of no more than 2.5, an accuracy of approximately 7.5 cm can be expected for the kinematic orbits of the BDS-3 MEO and IGSO/GEO satellites.

4.2. Single-satellite solution

To evaluate the applicability of the kinematic method for the BDS-3 constellation, we first investigated the kinematic orbits for each satellite except for C60 and C61 are determined in the ‘single-satellite’ mode, which refers to only determining the orbit of one satellite by fixing the orbits of the remaining satellites to the precise product. Fig. 6 illustrates the RMS of orbit differences between the determined kinematic and the reference dynamic solutions for all satellites during DOY 171–177, 2020. The orbital planes are distinguished by different colors. Generally, the mean 3D RMS of MEO satellites is 13.6 cm, compared to 23.5 cm and 33.7 cm for IGSO and GEO satellites, respectively. The relatively poorer observation geometry of IGSO and GEO satellites results in an accuracy reduction of approximately 10 cm. The mean along-track, cross-track and radial accuracy equals 9.7 cm, 7.3 cm, and 8.8 cm, respectively, for all BDS-3 satellites.

It can also be observed that the accuracy performance of MEO satellites across the three orbital planes is different. Satellites in Plane-B exhibit the highest accuracy, as the orbit accuracies of C43 and C44 in Plane-A and C25 and C26 in Plane-C lower the overall statistics for those planes. To investigate this reason, we analyze the POD residuals, as seen in Fig. 7. It is clear that the residuals of C25, C26, C43 and C44 are more than 8.8 cm, surpassing those of most MEO satellites. For IGSO and GEO satellites, although the measurement noise is not significant, the POD residuals are relatively large. This may be due to their poor observation geometry.

Table 2
Characteristics of kinematic method.

Component	Kinematic method
Solar radiation pressure (SRP)	Not needed
Antenna thrust	Not needed
Earth albedo	Not needed
Geopotential	Not needed
Third-body	Not needed
Tropospheric delay	Not needed
Ionospheric delay	Not needed
Ka-band PCO	manufacture values
Attitude model	SECM: proposed by Yang et al. [32] CAST: proposed by Wang et al. [31]
Relativistic effects	IERS Conventions 2010
Estimated parameters	Hardware delays, satellite position

Fig. 8 presents the timeseries of orbit differences between the computed kinematic and the dynamic orbits for MEO satellites. We select C27, C19 and C23 from the Plane-A, Plane-B and Plane-C, respectively. The measurements count per epoch is also illustrated. For C19 and C23, it is obvious that when the count of ISL observations is less than 5, the accuracy of orbits degenerates to above 40 cm. When the count of ISL observations is in the range of 10–15, the accuracy of orbit solutions varies with the count of observations. In most cases, reliable MEO orbits can be obtained with the 15 ISL observations. Notably, the accuracy of C27 does not drop dramatically with less than 10 observations. The accuracy of C23 kinematic orbits is lower than that of C19 and C27 due to the relatively large observation noise, as shown in Fig. 5. The radial orbit differences demonstrate noticeable bias. This indicates that there are some systematic errors, possibly due to the uncertainty of phase center offsets.

The timeseries of orbit differences and the count of observations for the three IGSO satellites are illustrated in Fig. 9. The 3D differences of C38 and C40 vary from 0 cm to 50 cm, while that of C39 only varies from 0 cm to 25 cm. And the 3D differences of C38 and C40 present a 12-h pattern. This could be associated with the orbital period. Although the PDOP of the three IGSO satellites is nearly identical, the 120° difference in the right ascension of the ascending node results in varying observation conditions in the northern and southern hemispheres. Consequently, each satellite shows a distinct pattern. Our research findings partially validate the analysis conducted by Gill [33]. Compared with the other two directions, the difference in the radial direction for IGSO satellites does not seem to be very sensitive to the change in the number of observations. When the count of observations for C40 is approximately 5, the cross-track accuracy deteriorates significantly. Even when increasing the number of observations from 15 to 20, the resulting orbit remains comparable in accuracy.

Noticeable systematic bias can also be observed in the radial direction for C39 and C40. In addition, there are considerable three-cycle-per-revolution (CPR) periodic variations in the radial orbits for C38 and C40, whereas C39 does not exhibit this phenomenon. Because the orbit and clock are strongly correlated, deficiencies in the orbit model can be reflected in the clock fitting residuals. As illustrated in Fig. 10, an analysis of the reference clock suggests that these errors may stem from the orbit dynamic model.

Fig. 11 depicts the timeseries of orbit differences and counts of observations for C59. Noticeable 1-CPR errors can be identified in the along-track and cross-track directions, whereas the radial orbits show pronounced 3-CPR variations. In addition, the amplitude of the orbit differences is larger in the first half day than in the second half day. However, it remains stable in the radial direction. Because there are more than 10 ISL observations available most of the time, the orbit errors reveal low dependency on the number of measurements.

4.3. Multi-satellite solution

In the above, the kinematic orbits are determined for each satellite by fixing that of the rest. However, it has lower practical usage, as the orbits for all satellites usually cannot be precisely obtained. In this subsection, the performance of kinematic orbits determined for multiple satellites simultaneously is investigated. This is termed as the ‘multi-satellite solution’ in this study. When all satellites' orbits are determined at the same time, the absolute orbits cannot be precisely obtained, as the datum for orientation is missing. Hence, anchor stations are introduced to solve this problem [34,35]. However, anchor station data for BDS-3 is not available. Hence, in this study, we attempt to fix the precise orbits of

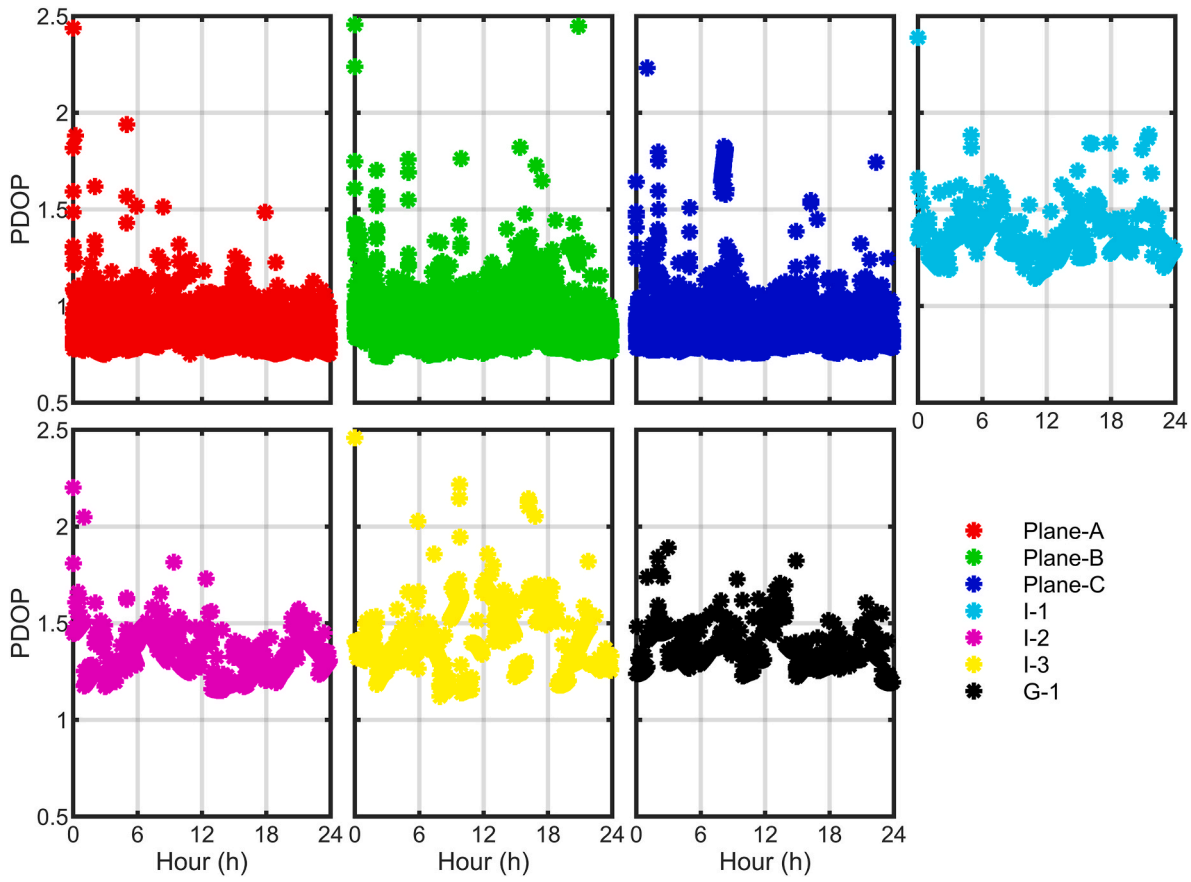

Fig. 4. PDOP timeseries of BDS-3 satellites in various orbital planes (red, Plane-A; green, Plane-B; blue, Plane-C), three IGSO (cyan, C38; purple, C39; yellow, C40), and GEO C59 (dark) on DOY 171, 2020. (For interpretation of the references to color in this figure legend, the reader is referred to the Web version of this article.)

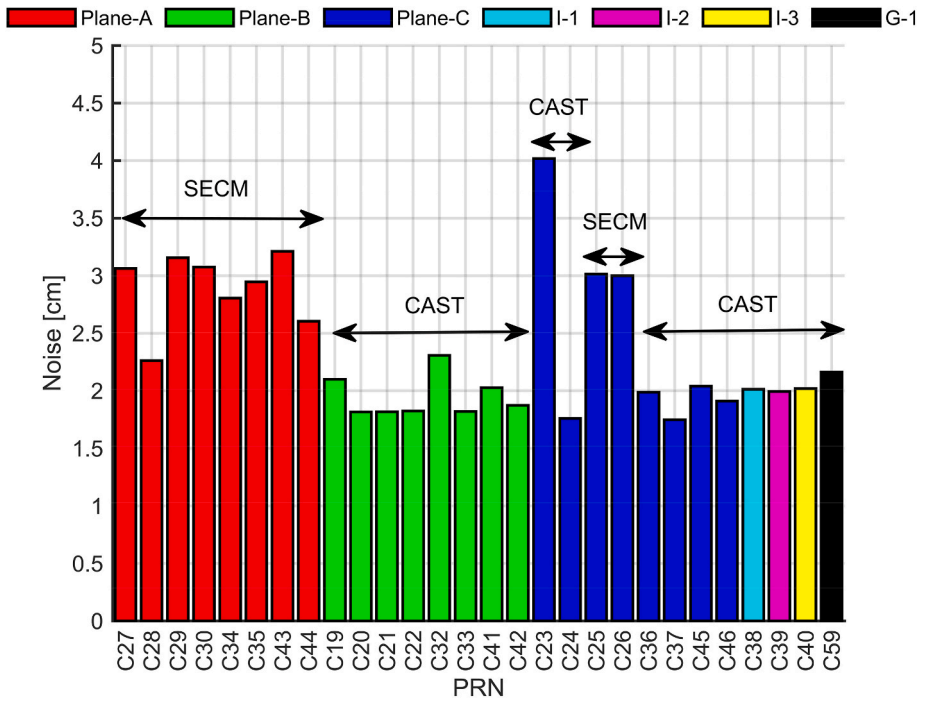

Fig. 5. ISL measurement noise for BDS-3 satellites across various orbital Planes.

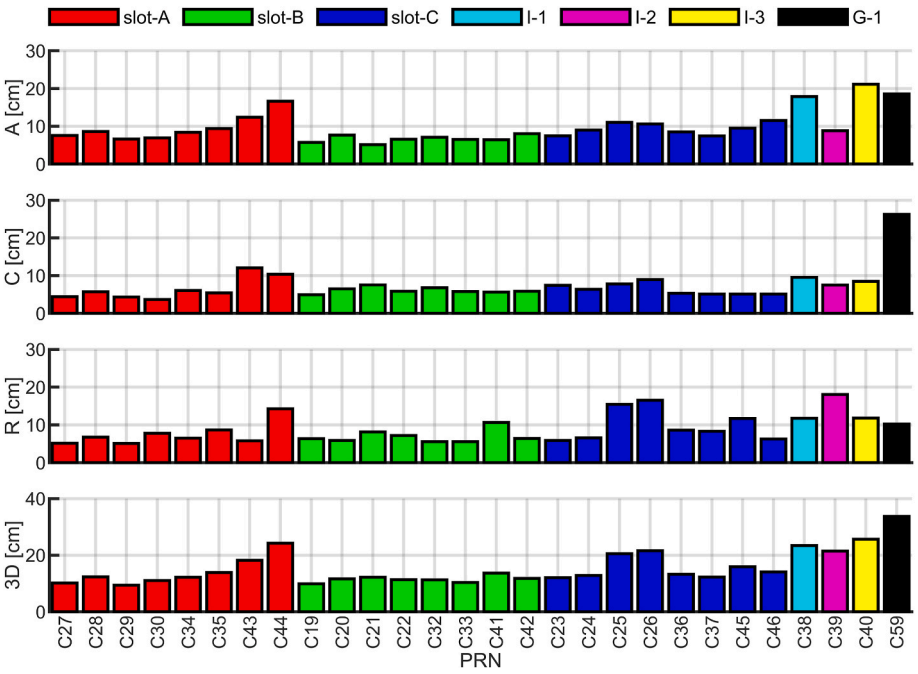

Fig. 6. RMS of orbit differences between the determined kinematic and reference dynamic solutions in the along-track (A), cross-track (C), radial (R) directions, and 3D for BDS-3 satellites during DOY 171–177, 2020.

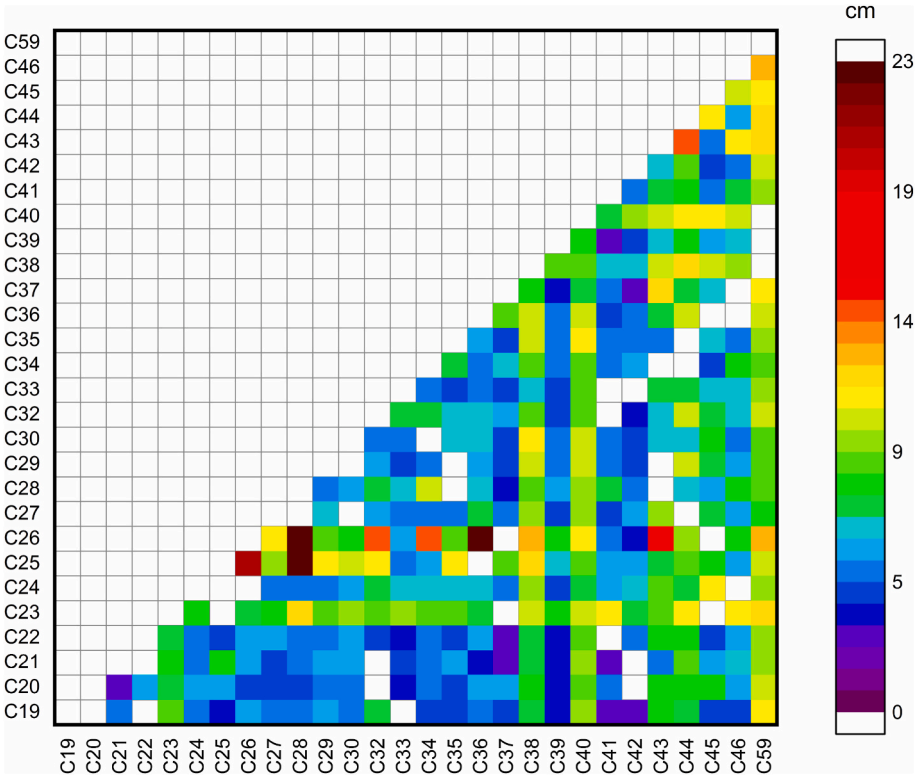

Fig. 7. RMS of ISL residuals for BDS-3 satellites during DOY 171–177, 2020.

a few satellites to overcome this issue. For the precise orbits determined with ground L-band data, as the monitoring stations of BDS are in China, the regional tracking condition for MEO and GEO is much poorer than that of IGSO satellites. Hence, we perform a series of solutions using different IGSO satellites as the datum to find the optimum option of kinematic orbits.

Table 3 summarizes the RMS statistics of orbit differences between the kinematic and dynamic orbit solutions for BDS-3 satellites during DOY 171–177, 2020. The solutions SA1-C38, SA2-C39, and SA3-C40 are obtained by fixing the orbits of C38, C39, and C40, respectively. Generally, the mean 3D RMS values are increased by factors of 3–4, 2–3, and 1–2 for MEO, IGSO, and GEO satellites, respectively, than those of single-satellite solutions. The performance of the three solutions is similar. The best solution is SA1-C38 with the mean RMS of all satellites

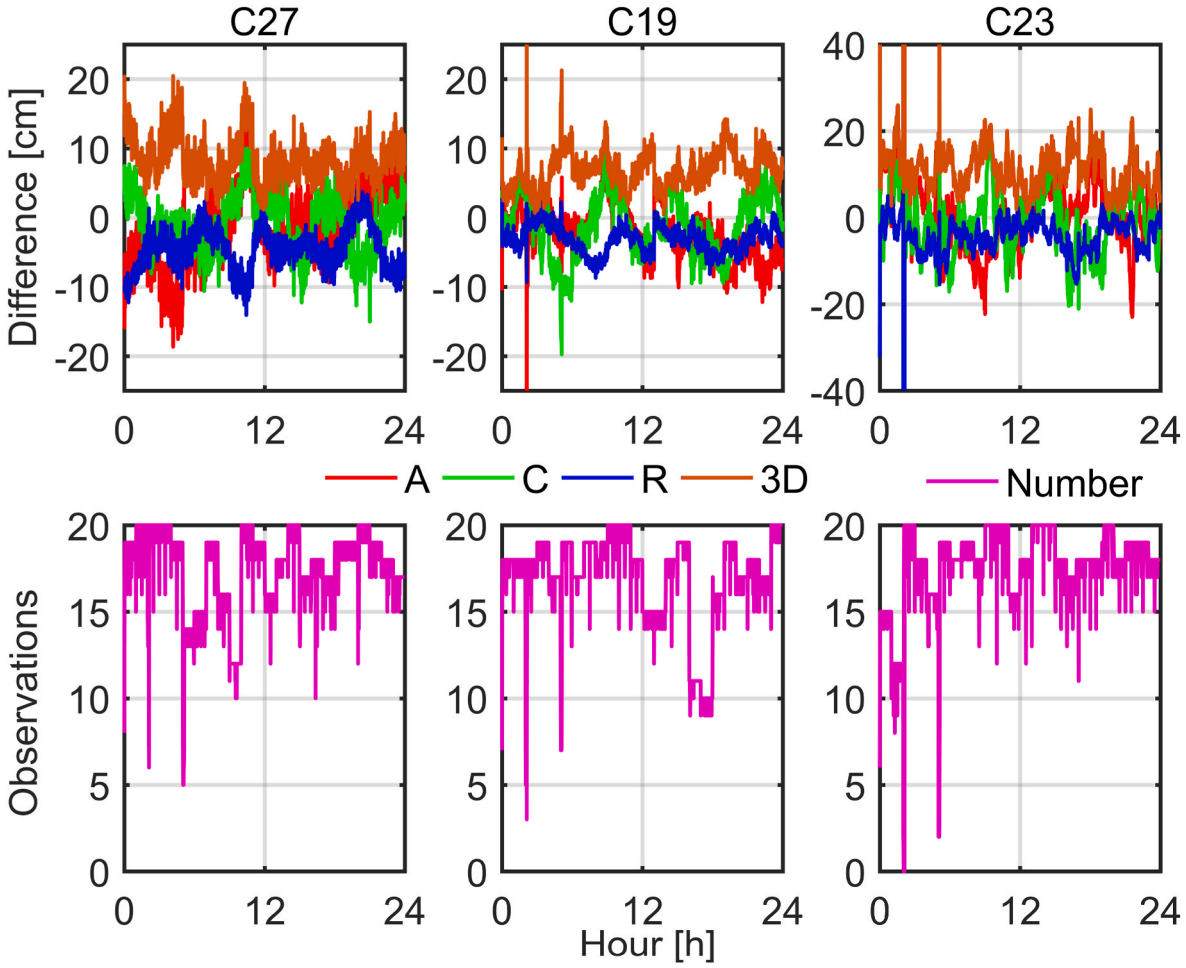

Fig. 8. Timeseries of orbit differences (top) and the count of observations (bottom) for selected MEO satellites (C27, C19 and C23), representing the A, B, and C orbital planes, on DOY 171, 2020. Please be aware that C23 has a different vertical axis scale.

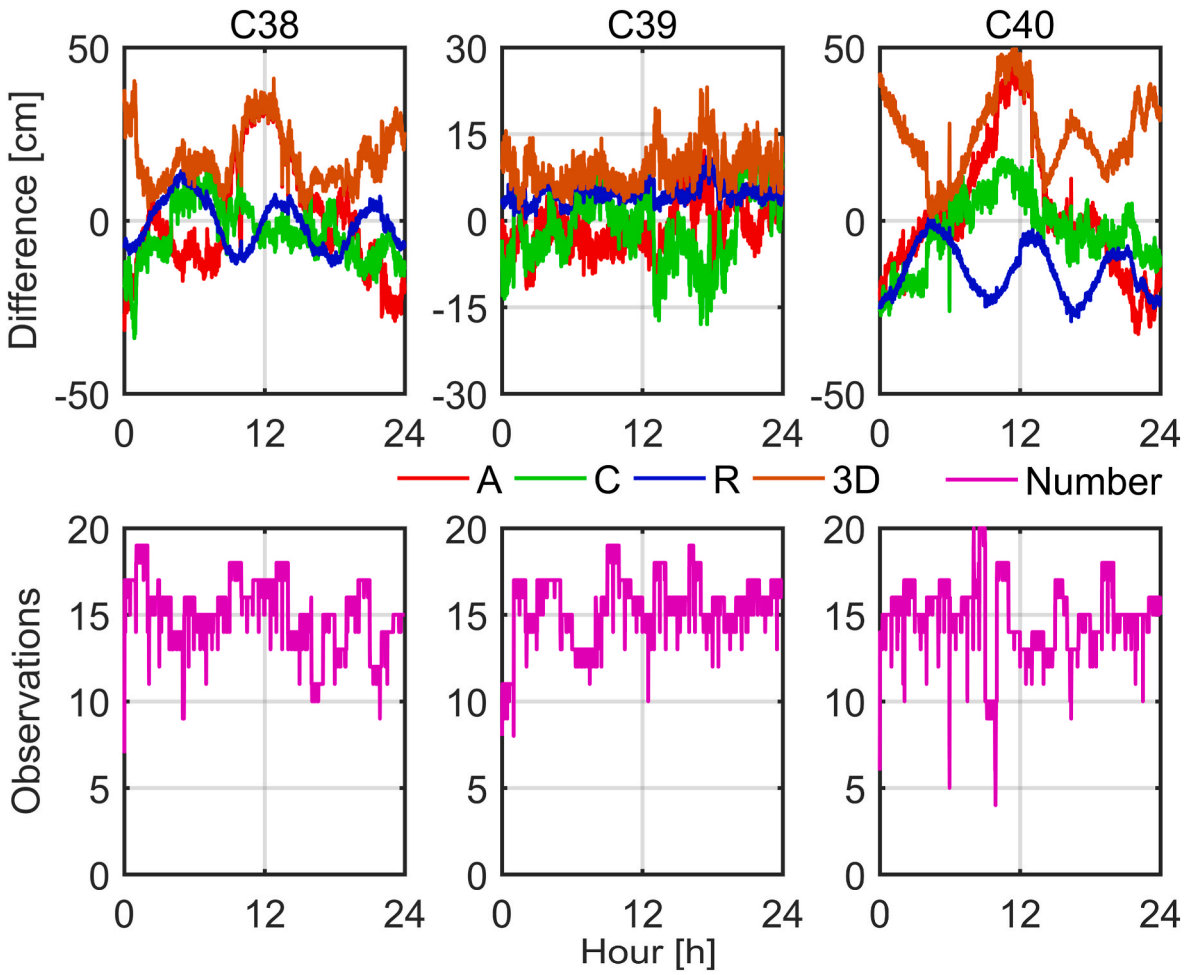

Fig. 9. Timeseries of orbit differences (top) and the number of observations (bottom) for three IGSO satellites on DOY 171, 2020. Please be aware that C39 has a different vertical axis scale.

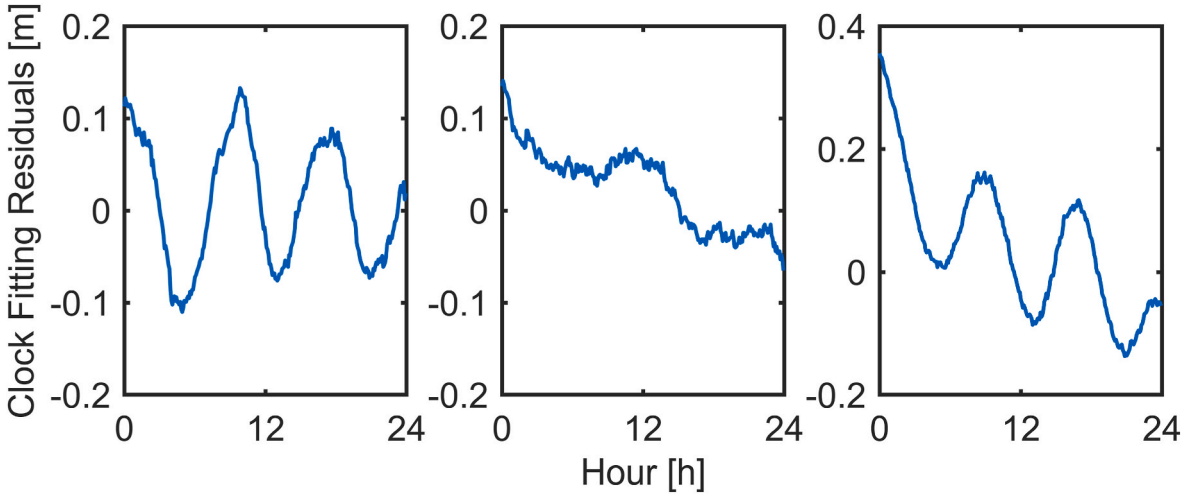

Fig. 10. Timeseries of reference clock fitting residuals of C38 (left), C39 (middle), and C40 (right) on DOY 171, 2020.

at the levels of 35.9, 34.9 and 17.1 cm for the along-track, cross-track and radial components, respectively. The along-track and cross-track RMS values for the three solutions are higher than the radial RMS value because the geometric constraint in the radial direction is stronger. Furthermore, except for SA3-C40, the results of the satellites in the Plane-B are marginally superior to those in the Plane-A and Plane-C.

Because the accuracy of kinematic orbit solutions with one IGSO satellite as the datum is not as good as expected, the solutions obtained by fixing two IGSO satellites are determined. Hence, three new solutions are obtained, with corresponding results are presented in Table 4. The mean 3D RMS errors of the three solutions are 40.4, 45.6, and 39.2 cm, respectively, and its accuracy was improved by at least 7.9 cm with

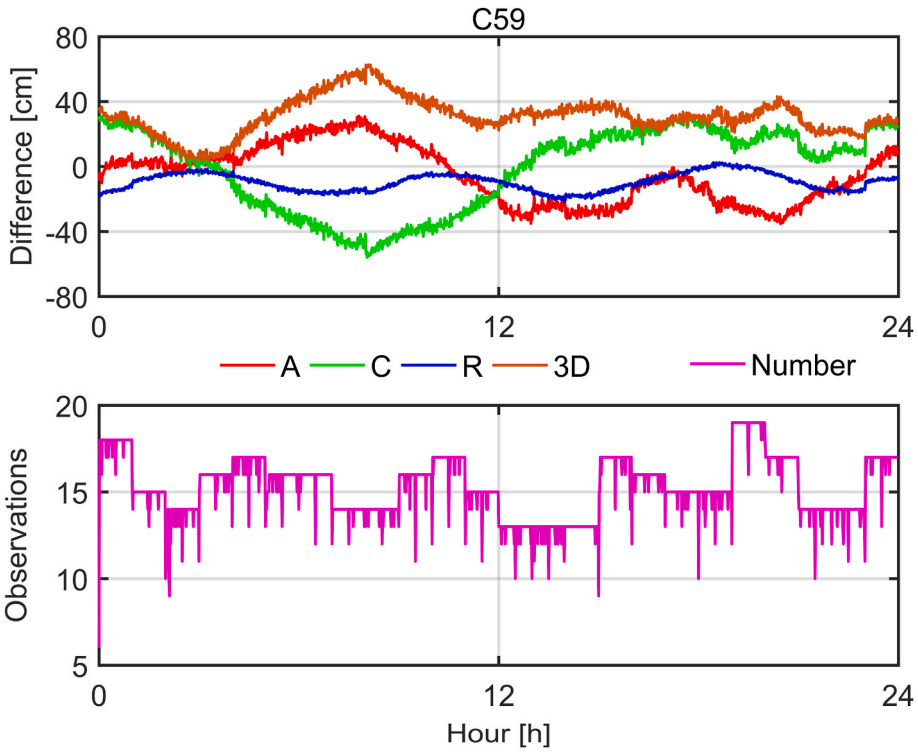

Fig. 11. Timeseries of the difference (top) and counts of observations (bottom) for C59 on DOY 171, 2020.

Table 3
The accuracy of the kinematic orbit solutions. (unit: cm).

	SA1-C38				SA2-C39				SA3-C40			
Plane	Alo.	Cro.	Rad.	3D	Alo.	Cro.	Rad.	3D	Alo.	Cro.	Rad.	3D
Plane-A	30.9	37.0	16.5	51.0	40.6	32.4	18.2	55.1	32.1	38.8	17.5	53.4
Plane-B	29.8	36.6	17.0	50.3	28.4	36.6	18.6	50.0	41.6	31.8	17.3	55.2
Plane-C	42.6	30.1	18.7	55.6	33.9	34.4	21.4	53.0	33.5	36.2	20.8	53.7
IGSO	47.1	42.1	14.4	64.8	48.8	35.7	20.9	64.5	50.9	35.1	19.4	64.9
GEO	50.5	27.3	16.0	59.6	52.1	37.2	26.2	69.2	45.8	40.7	23.6	65.7
ALL	35.9	34.9	17.1	53.5	36.0	34.7	19.8	54.2	37.2	35.8	18.8	55.3

Table 4
The accuracy of the kinematic orbit solutions by fixing two IGSO satellite orbits. SB1-C38C39, SB2-C39C40 and SB3-C38C40 are solutions for fixing the orbits of C38 and C39, C39 and C40, as well as C38 and C40, respectively. (unit: cm).

	SB1-C38C39				SB2-C39C40				SB3-C38C40			
Plane	Alo.	Cro.	Rad.	3D	Alo.	Cro.	Rad.	3D	Alo.	Cro.	Rad.	3D
Plane-A	24.9	24.9	19.0	40.1	25.4	31.3	20.2	45.2	29.6	18.8	20.1	40.5
Plane-B	21.8	27.5	17.0	39.1	27.5	28.5	20.4	44.6	19.2	26.4	18.0	37.4
Plane-C	28.2	21.4	21.6	41.6	31.8	23.9	24.5	46.9	22.5	25.1	20.8	39.7
IGSO	38.6	15.9	16.8	45.0	39.8	15.7	21.1	47.7	17.4	24.8	17.7	35.0
GEO	19.1	28.4	19.7	39.5	23.4	27.3	25.0	43.8	21.2	29.5	22.7	42.9
ALL	25.2	24.4	19.2	40.4	28.5	27.4	21.8	45.6	23.4	23.7	19.7	39.2

respect to that of the solutions in Table 3. When one more reference satellite is added, the along-track and cross-track RMS values decrease dramatically. This shows that adding one more constraint effectively suppresses the error along the these directions. The satellites in the B plane exhibit the smallest RMS values among all MEO planes. The accuracy of the IGSO and GEO satellites increases by at least 15 cm compared with the three SA solutions.

Furthermore, Table 5 lists the kinematic solutions obtained by fixing all IGSO orbits, with the mean 3D RMS for all satellites being 39.2 cm. It is surprising that the solution shows similar performance to the above solutions by fixing the two-satellite orbits. The mean RMS of MEO

Table 5
The accuracy of the kinematic orbit solutions by fixing all IGSO satellite orbits. (unit: cm).

Plane	Alo.	Cro.	Rad.	3D
Plane-A	25.7	21.9	20.4	39.5
Plane-B	19.4	27.6	17.7	38.1
Plane-C	25.1	19.6	24.3	40.2
GEO	19.0	25.5	19.5	37.3
ALL	23.2	23.2	20.7	39.2

Table 6
The accuracy of the kinematic orbit solutions fixing all IGSO and GEO satellites. (unit: cm).

Plane	Alo.	Cro.	Rad.	3D
Plane-A	17.8	13.2	13.7	26.1
Plane-B	12.8	16.8	11.8	24.4
Plane-C	16.8	13.3	16.6	27.2
ALL	15.8	14.5	14.0	25.9

satellites in the along-track, cross-track and radial directions are at the level of approximately 20 cm. The orbit accuracy of satellites on various orbital planes is comparable. Similar accuracy is also observed for GEO.

In addition, the solution taking all the IGSO and GEO satellites as the datum is also investigated. As shown in Table 6, this solution with the best accuracy in all the multi-satellites strategies can be noticed. The mean RMS of all satellites equals 15.8, 14.5, and 14.0 cm in the along-track, cross-track, and radial direction, respectively. The orbit quality of the spacecraft on the B plane is slightly superior to that of satellites on the other planes. This is attributable to the lower ISL measurement noise observed for satellites in Plane-B.

5. The performance of kinematic orbits in the eclipse seasons

For the dynamic orbits, the accuracy degenerates in the eclipse seasons due to the yaw attitude maneuvers as well as the deficiency of the non-conservative force models. However, for kinematic orbits, which are free of dynamic perturbation, it is expected that the orbit accuracy remains stable in and out of the eclipse seasons. To evaluate this, the kinematic orbit solution from DOY 125 to 165 in 2020 is determined. During this period, the satellites of Plane-C are in eclipse seasons, with the Sun elevation angle varying from -18.2° to 17.8°.

Fig. 12 illustrates the daily RMS of the single-satellite solution for the spacecraft. The daily along-track and cross-track RMS are less than 20 cm, with an exception of C25, C26, and C45. This may be related to the measurement noise (as shown in Figs. 5 and 7) and the observation geometry. According to Chen et al. [36], the along-track orbit overlapping errors of CAST satellites can increase by up to 80 cm in the eclipse period. While the orbit quality of satellites in Plane-C does not show obvious degradation during the Earth shadow period.

6. Conclusion and discussion

One significant benefit of BDS-3 is equipping each satellite with a Ka-band array antenna for inter-satellite ranging and communication, thus providing a new way for orbit determination. We implement kinematic orbit determination by only using BDS-3 ISL observations in this study. The single-satellite and multi-satellite solutions are investigated to obtain better solutions.

The PDOP is obtained to assess the orbit accuracy in theory. Values of PDOP are smaller than 2 for MEO satellites most of the time, whereas the PDOP of IGSO and GEO satellites range from 1.2 to 2.5. Considering that the noise levels of BDS-3 satellites are between 1.8 and 4 cm, the theoretical accuracy of MEO, and IGSO as well as GEO satellites, are at the level of 7.5 cm. The single-satellite mode provides the best solution. For MEO satellites, the 3D accuracy is 13.6 cm, while it is 23.5 cm for IGSO satellites and 33.7 cm for GEO satellites.

In addition to the number of observations, the choice of satellites used as the datum also affects the kinematic orbit solution. For practicality, taking all IGSO satellites as references, the along-track, cross-track, and radial RMS values of multi-satellites solution equal 23.2, 23.2 and 20.7 cm, respectively. This is superior to the accuracy of the broadcast ephemeris evaluated by Lv et al. [16] in the along-track (44 cm) and the cross-track (40 cm) directions but inferior to the broadcast ephemeris in the radial (7 cm) direction.

Although it is difficult for GEO satellites to obtain high-quality orbits due to poor observation geometry, we can expect better results with the construction of BDS-4, i.e., the addition of LEO satellites. Hence, we explore kinematic orbits when using IGSO and GEO satellites as the datum. The accuracy in three directions can reach 15 cm. Additionally, the advantage of kinematic orbits is reflected in the consistent orbital accuracy maintained in and out of the eclipse seasons.

The discrepancy in accuracy between theoretical predictions and actual determinations may be attributed to the ISL measurement models, such as the range bias models and ISL antenna PCOs. Refining

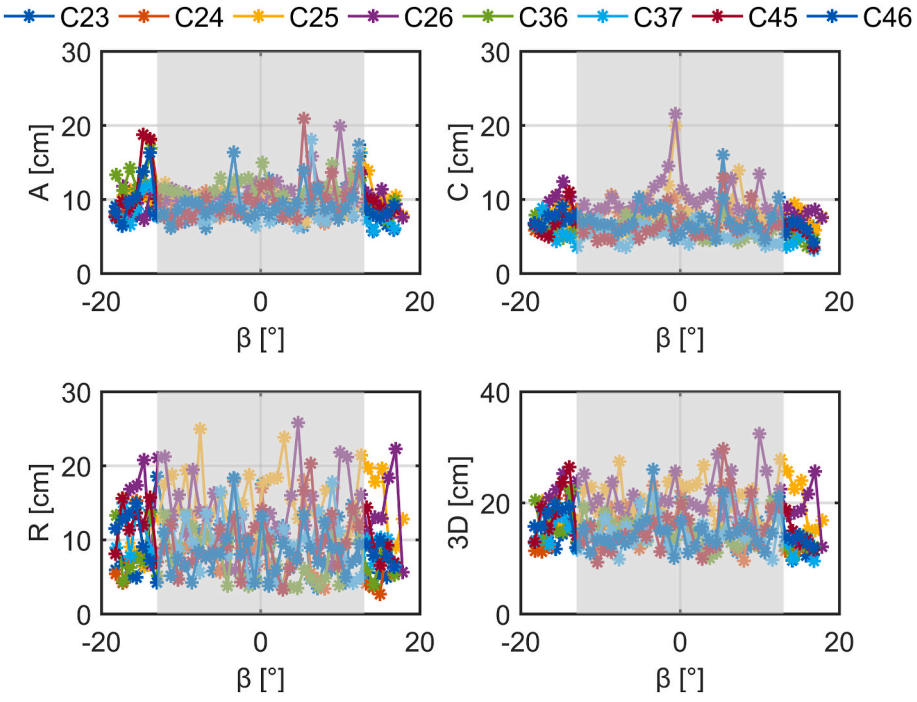

Fig. 12. Timeseries of the daily RMS for satellites in orbital Plane-C during DOY 125–165, 2020. The eclipse period is represented by the shaded area.

these models is likely to lead to further improvements. Future GNSS constellations with LEO satellites will be equipped with optical ISLs, providing high-precision data and improved observation geometry, which would also benefit the accuracy of kinematic orbits for GNSS satellites.

CRediT authorship contribution statement

Chao Yang: Writing – review & editing, Writing – original draft, Visualization, Validation, Formal analysis, Data curation, Conceptualization. **Jing Guo:** Writing – review & editing, Writing – original draft, Conceptualization. **Xiaolong Mi:** Visualization, Validation. **Yuanfan Deng:** Visualization, Validation. **Xuexi Liu:** Visualization, Validation. **Qile Zhao:** Visualization, Validation. **Wu Chen:** Visualization, Validation.

Funding declaration

This study is financially supported by the General Research Fund of Hong Kong (Grant No. 15229622), the National Natural Science Foundation of China (42574044, 42030109, 42404052, 42304015), and the Natural Science Foundation of Jiangsu Province (BK20231087). The numerical calculations in this paper have been done on the supercomputing system in the Supercomputing Center of Wuhan University.

Declaration of competing interest

The authors declare that they have no known competing financial interests or personal relationships that could have appeared to influence the work reported in this paper.

Acknowledgment

The IGS and iGMAS are acknowledged for providing the satellite ephemeris and ground L-band tracking data. We also thank CSNO for proving ISL data.

References

[1] M.P. Ananda, H. Bernstein, K.E. Cunningham, W.A. Feess, E.G. Stroud, Global positioning system (GPS) autonomous navigation, in: IEEE Symposium on Position Location and Navigation. A Decade of Excellence in the Navigation Sciences, 1990, pp. 497–508, https://doi.org/10.1109/PLANS.1990.66220.
[2] S.C. Fisher, K. Ghassemi, GPS IIF-the next generation, Proc. IEEE 87 (1999) 24–47, https://doi.org/10.1109/5.736340.
[3] J.A. Rajan, Highlights of GPS II-R autonomous navigation, pp. 354–363, http://www.ion.org/publications/abstract.cfm?jp=p&articleID=969, 2002. (Accessed 22 October 2022).
[4] K.P. Maine, P. Anderson, J. Langer, Crosslinks for the next-generation gps, in: 2003 IEEE Aerospace Conference Proceedings (Cat. No.03TH8652), 2003, https://doi.org/10.1109/AERO.2003.1235087, p. 4_1589-4_1596.
[5] F.A. Fernández, Inter-satellite ranging and inter-satellite communication links for enhancing GNSS satellite broadcast navigation data, Adv. Space Res. 47 (2011) 786–801, https://doi.org/10.1016/j.asr.2010.10.002.
[6] G. Giorgi, T.D. Schmidt, C. Trainotti, R. Mata-Calvo, C. Fuchs, M.M. Hoque, J. Berdermann, J. Furthner, C. Günther, T. Schuldt, J. Sanjuan, M. Gohlke, M. Oswald, C. Braxmaier, K. Balidakis, G. Dick, F. Flechtner, M. Ge, S. Glaser, R. König, G. Michalak, M. Murböck, M. Semmling, H. Schuh, Advanced technologies for satellite navigation and geodesy, Adv. Space Res. 64 (2019) 1256–1273, https://doi.org/10.1016/j.asr.2019.06.010.
[7] S. Glaser, G. Michalak, B. Männel, R. König, K.H. Neumayer, H. Schuh, Reference system origin and scale realization within the future GNSS constellation “kepler,”, J. Geod. 94 (2020) 117, https://doi.org/10.1007/s00190-020-01441-0.
[8] G. Michalak, S. Glaser, K.H. Neumayer, R. König, Precise orbit and Earth parameter determination supported by LEO satellites, inter-satellite links and synchronized clocks of a future GNSS, Adv. Space Res. 68 (2021) 4753–4782, https://doi.org/10.1016/j.asr.2021.03.008.
[9] H. Wang, Z. Chen, J. Zheng, H. Chu, A new algorithm for onboard autonomous orbit determination of navigation satellites, J. Navig. 64 (2011) S162–S179, https://doi.org/10.1017/S0373463311000397.
[10] S. Han, Q. Gui, J. Li, Establishment criteria, routing algorithms and probability of use of inter-satellite links in mixed navigation constellations, Adv. Space Res. 51 (2013) 2084–2092, https://doi.org/10.1016/j.asr.2012.12.020.
[11] Y. Xu, Q. Chang, Z. Yu, On new measurement and communication techniques of GNSS inter-satellite links, Sci. China Technol. Sci. 55 (2012) 285–294, https://doi.org/10.1007/s11431-011-4586-7.
[12] Y. Zhou, Y. Wang, W. Huang, J. Yang, L. Sun, In-orbit performance assessment of BeiDou intersatellite link ranging, GPS Solut. 22 (2018) 119, https://doi.org/10.1007/s10291-018-0784-0.
[13] X. Ren, Y. Yang, J. Zhu, T. Xu, Orbit determination of the next-generation beidou satellites with intersatellite link measurements and a priori orbit constraints, Adv. Space Res. 60 (2017) 2155–2165, https://doi.org/10.1016/j.asr.2017.08.024.
[14] J.P. Chen, H.U. Xiaogong, C.P. Tang, S.S. Zhou, R. Guo, J.Y. Pan, L.I. Ran, L.F. Zhu, Orbit determination and time synchronization for new-generation beidou satellites: preliminary results, Sci. Sin. (2016), https://doi.org/10.1360/SSPMA2016-00281.
[15] D. Yang, J. Yang, G. Li, Y. Zhou, C. Tang, Globalization highlight: orbit determination using BeiDou inter-satellite ranging measurements, GPS Solut. 21 (2017) 1395–1404, https://doi.org/10.1007/s10291-017-0626-5.
[16] Y. Lv, T. Geng, Q. Zhao, X. Xie, R. Zhou, Initial assessment of BDS-3 preliminary system signal-in-space range error, GPS Solut. 24 (2020) 16, https://doi.org/10.1007/s10291-019-0928-x.
[17] Y. Yang, Y. Yang, X. Hu, J. Chen, R. Guo, C. Tang, S. Zhou, L. Zhao, J. Xu, Inter-satellite link enhanced orbit determination for BeiDou-3, J. Navig. 73 (2020) 115–130, https://doi.org/10.1017/S0373463319000523.
[18] X. Xie, T. Geng, Q. Zhao, Y. Lv, H. Cai, J. Liu, Orbit and clock analysis of BDS-3 satellites using inter-satellite link observations, J. Geod. 94 (2020) 64, https://doi.org/10.1007/s00190-020-01394-4.
[19] L. He, T. Sun, H. Wang, Y. Zhou, Z. Wang, X. He, A novel non-conservative perturbation model for enhanced precise orbit determination of BDS-3 SECM satellites, Measurement (2025) 116915, https://doi.org/10.1016/j.measurement.2025.116915.
[20] C. Yang, J. Guo, X. Xu, L. Wang, Q. Zhao, Impacts of inter-satellite links on the ECOM model performance for BDS-3 MEO satellites, Satell Navig 5 (2024) 14, https://doi.org/10.1186/s43020-024-00131-y.
[21] S. Xie, G. Huang, L. Wang, H. She, W. Lai, M. Wang, Enhancing empirical SRP model for BDS-3 MEO satellites via semi-analytical accelerations analysis, Acta Astronaut. 228 (2025) 792–802, https://doi.org/10.1016/j.actaastro.2024.12.044.
[22] Y. Lv, T. Geng, Q. Zhao, X. Xie, F. Zhang, X. Wang, Evaluation of BDS-3 orbit determination strategies using ground-tracking and inter-satellite link observation, Remote Sens. 12 (2020) 2647, https://doi.org/10.3390/rs12162647.
[23] C. Yang, J. Guo, X. Xu, L. Wang, Q. Zhao, Solar radiation pressure models for BDS-3 IGSO: impacts and improvement from observation geometry, Meas. Sci. Technol. 36 (2025) 036308, https://doi.org/10.1088/1361-6501/ad9e0c.
[24] F. Jiao, Y. Hu, X. Yu, H. Wang, Q. Chen, Geostationary autonomous trajectory determination technology based on enhanced inter-satellite links of the beidou medium earth orbit constellation, Aero. Sci. Technol. 163 (2025) 110240, https://doi.org/10.1016/j.ast.2025.110240.
[25] D. Švehla, M. Rothacher, Kinematic and reduced-dynamic precise orbit determination of low earth orbiters, Adv. Geosci. 1 (2003) 47–56, https://doi.org/10.5194/adgeo-1-47-2003.
[26] D. Švehla, M. Rothacher, Kinematic positioning of LEO and GPS satellites and IGS stations on the ground, Adv. Space Res. 36 (2005) 376–381, https://doi.org/10.1016/j.asr.2005.04.066.
[27] C. Tang, X. Hu, S. Zhou, L. Liu, J. Pan, L. Chen, R. Guo, L. Zhu, G. Hu, X. Li, F. He, Z. Chang, Initial results of centralized autonomous orbit determination of the new-generation BDS satellites with inter-satellite link measurements, J. Geod. 92 (2018) 1155–1169, https://doi.org/10.1007/s00190-018-1113-7.
[28] J. Guo, X. Xu, Q. Zhao, J. Liu, Precise orbit determination for quad-constellation satellites at Wuhan University: strategy, result validation, and comparison, J. Geod. 90 (2016) 143–159, https://doi.org/10.1007/s00190-015-0862-9.
[29] C. Wang, Q. Zhao, J. Guo, J. Liu, G. Chen, The contribution of intersatellite links to BDS-3 orbit determination: model refinement and comparisons, Navigation 66 (2019) 71–82, https://doi.org/10.1002/navi.295.
[30] J. Liu, M. Ge, PANDA software and its preliminary result of positioning and orbit determination, Wuhan Univ. J. Nat. Sci. 8 (2003) 603, https://doi.org/10.1007/BF02899825.
[31] C. Wang, J. Guo, Q. Zhao, J. Liu, Yaw attitude modeling for BeiDou I06 and BeiDou-3 satellites, GPS Solut. 22 (2018) 117, https://doi.org/10.1007/s10291-018-0783-1.
[32] C. Yang, J. Guo, Q. Zhao, Yaw attitudes for BDS-3 IGSO and MEO satellites: estimation, validation and modeling with intersatellite link observations, J. Geod. 97 (2023) 6, https://doi.org/10.1007/s00190-022-01698-7.
[33] E. Gill, Precise GNSS-2 satellite orbit determination based on inter-satellite-links. 14th International Symposium on Space Flight Mechanics, 1999, p. 9.
[34] J.A. Rajan, P. Brodie, H. Rawicz, Modernizing GPS autonomous navigation with anchor capability, pp. 1534–1542, http://www.ion.org/publications/abstract.cfm?jp=p&articleID=5338, 2003. (Accessed 13 June 2022).
[35] H. Yi, B. Xu, Y. Gao, J. Wang, Long-term semi-autonomous orbit determination supported by a few ground stations for navigation constellation, Sci. China Phys. Mech. Astron. 54 (2011) 1342–1353, https://doi.org/10.1007/s11433-011-4373-2.
[36] X. Chen, M. Ge, Y. Liu, L. He, H. Schuh, Adapting empirical solar radiation pressure model for BDS-3 medium Earth orbit satellites, GPS Solut. 27 (2023) 183, https://doi.org/10.1007/s10291-023-01524-3.